



Rapid dissociation of high concentration excitons between $[\text{Bi}_2\text{O}_2]^{2+}$ slabs with multifunctional N-Bi-O sites for selective photoconversion into CO

Guosheng Zhou^{a,b,c}, Yangrui Xu^{b,c}, Yu Cheng^b, Zehui Yu^b, Binghui Wei^b, Xinlin Liu^d, Ziran Chen^e, Chunxiang Li^a, Ziyang Lu^{b,c,f,*}

^a Institute of the Green Chemistry and Chemical Technology, School of Chemistry and Chemical Engineering, Jiangsu University, Zhenjiang 212013, Jiangsu, PR China

^b School of Emergency Management, Institute of Environmental Health and Ecological Security, School of the Environment and Safety Engineering, Jiangsu University, Zhenjiang 212013, Jiangsu, PR China

^c State Key Laboratory of Structural Chemistry, Fujian Institute of Research on the Structure of Matter, Chinese Academy of Sciences, Fuzhou, Fujian 350002, PR China

^d School of Energy and Power Engineering, Jiangsu University, Jiangsu 212013, China

^e Department of Architecture and Environment Engineering, Sichuan Vocational and Technical College, Suining, Sichuan 629000, PR China

^f Jiangsu Collaborative Innovation Center of Technology and Material of Water Treatment, Suzhou University of Science and Technology, Suzhou 215009, Jiangsu, PR China

ARTICLE INFO

Keywords:

High concentration excitons dissociation

$[\text{Bi}_2\text{O}_2]^{2+}$ slabs

Multifunctional N-Bi-O sites

Holes

Photoconversion into CO

ABSTRACT

Regulation of exciton generation and dissociation, directed transfer to active center and oxidation capacity are the key steps in photoconversion. Here, we report that the multifunctional N-Bi-O sites are prepared in BiOBr nanosheets without the introduction of oxygen vacancy to reduce localized overreaction centers, which can not only enhance the Coulomb force between $[\text{Bi}_2\text{O}_2]^{2+}$ slabs, thus increasing the exciton concentration, but also form low-oxidation-state active centers which can serve as the selective reaction sites and hole capture sites. Additionally, electronic fast recombination channels promote rapid dissociation of excitons and synergistic attraction to low-oxidation-state active centers to form weak holes. These holes prefer to rapid photoconversion of TC into CO instead of CO_2 . The yield of selective photoconversion into CO is $43.53 \mu\text{mol/g}$, and the proportion of CO products is 16.21%. This work proposes a strategy for the cooperative construction of multifunctional active centers and multiexciton dissociation structures.

1. Introduction

The increasing energy demand and natural environmental pollution, semiconductor-based photoconversion technology seems to be considered as a promising sustainable strategy [1–4]. In different application scenarios, it can not only be used in photocatalytic CO_2 reduction, H_2O decomposition, organic synthesis and other fields, but also produce various free radicals to decompose pollutants [5–7]. However, the photocatalytic degradation of pollutants is dominated by oxidation, which inevitably leads to the complete oxidation of pollutants and produces a large amount of CO_2 , which becomes an emission source of greenhouse gases. This could seriously hamper progress towards carbon neutrality. Therefore, the conversion of pollutants into chemical fuels is a promising way to solve the problem of pollutant removal and CO_2 emission reduction, but also to produce high value products such as

carbon monoxide and acetic acid [8–11]. Appropriate modification of photocatalyst is very important to improve the performance of specific application scenarios [12–15]. It is generally considered that the effective separation of space electrons (e^-) and holes (h^+) is the decision-making step of photocatalytic performance, because photo-excited electrons are easy to combine with holes in a few picoseconds, and separation means that more carriers migrate quickly [16]. Therefore, the separation of e^- and h^+ is taken as the research focus, but the exciton effect mediated by the Coulomb force interaction between e^- and h^+ has long been ignored in the photocatalytic process. In particular, low dimensional semiconductors have significant exciton effect, which is due to the reduction of dielectric constant and weak shielding effect due to limited size [17]. Excitons are bound e^-h^+ pairs, which are separated in space but entangled in energy, which greatly hinders the dissociation of excitons and the generation of charge carriers, resulting

* Corresponding author at: School of Emergency Management, Institute of Environmental Health and Ecological Security, School of the Environment and Safety Engineering, Jiangsu University, Zhenjiang 212013, Jiangsu, PR China.

E-mail address: luziyang126@126.com (Z. Lu).

<https://doi.org/10.1016/j.apcatb.2023.122892>

Received 10 March 2023; Received in revised form 10 May 2023; Accepted 17 May 2023

Available online 18 May 2023

0926-3373/© 2023 Elsevier B.V. All rights reserved.

in low photocatalytic activity. Therefore, in order to fully understand the photocatalytic process, it is necessary to consider the exciton effect of low dimensional semiconductors widely.

Strong exciton effect will make photoexcited electrons migrate to exciton-mediated trap state to form bound electron-hole pairs and release part of their energy, which will also reduce the rapid recombination of photogenerated electrons and holes, and promote the improvement of photoexcited ability [18–21]. The exciton binding energy (E_b) is the energy required for exciton dissociation to form free carriers, and the E_b value represents the coulomb interaction strength and exciton stability. According to the Saha–Langmuir equation, a larger E_b value can achieve a higher exciton concentration environment [19]. However, too large E_b value will also lead to the rapid annihilation of excitons. This also suggests that besides the premise of increasing exciton concentration, the construction of exciton dissociation system is also very important.

For increasing exciton concentration, in addition to reducing the thickness of the low dimensional semiconductor to reduce the exciton shielding effect and enhance E_b , increasing the localized electron density at the edge of the conduction and valence bands is also a powerful means [17]. The high charge density at the edge of the band gap helps more photoexcited electrons to transition, which has been shown to be achieved through nonmetallic orbital hybridization or other means. As a nonmetallic orbital hybridization formed by a nonmetal-metal-oxygen site structure, N element has a low electronegativity, which can form a new energy level above the valence band energy level through orbital hybridization with surrounding metal and oxygen elements, effectively reduce the band gap, and improve the edge charge density of the valence band, so as to promote stronger visible light absorption capacity. Noted that the formation of higher reaction energy level positions helps to reduce the oxidation of holes, which can help to control the oxidation of holes in the photoconversion process and prevent the feedstock from being over-oxidized to form by-products such as CO_2 [16,22–27]. However, the conventional preparation methods of N-metal-O sites, such as ammonia calcination, lead to the instability of the structure and easily introduce a large number of defects, thus forming N-metal-vacancy sites, which will form disordered electron localization structure and inappropriate active reaction sites, leading to overreaction [28,29]. Therefore, it is necessary to explore an appropriate method to reduce the formation of oxygen vacancies while forming N-metal-O sites [30]. Besides, the formation of N-metal-O sites are also conducive realization of rapid directional migration of free carriers, and the improvement of photocatalytic efficiency [31,32]. According to our previous research, the N-Cd-O active centers prepared by target molecular transformation engineering can effectively serve as the reaction site of TC molecules [33]. It can be expected that N-metal-O sites as the reactive sites are more conducive to photoconversion. Therefore, as an excellent modification method, N-metal-O sites can not only improve the localized density of valence band-edge electrons to increase the exciton concentration, but also construct appropriate low-oxidation-state active centers.

On the other hand, conventional exciton dissociation usually forms the area of disordered energy landscape by constructing defects, boronizing the surface, constructing an ordered-disordered interface, and metal doping, which is similar to an electrons trap to promote the rapid dissociation of excitons [34–36]. However, these methods will strongly change the distribution of charge in the matrix material, and greatly affect the coulomb interaction between photoexcited electrons and holes to reduce E_b value. Therefore, the construction of heterojunction is a suitable method to separate excitons using electron fast channels between interfaces without changing the energy level structure of the matrix material [21,37–41]. In order to better understand the exciton generation and deionization mechanism, we focus on BiOBr, because the simultaneous charge localization of the conduction band and valence band near the band edge of confined $[\text{Bi}_2\text{O}_2]^{2+}$ slabs are beneficial to the e^- and h^+ interaction, which greatly affects the exciton behavior in the

photocatalytic process [17,35]. Besides, $[\text{Bi}_2\text{O}_2]^{2+}$ slab, as an excellent platform for exciton effect research, is not only easy to modify but also easy to construct heterojunction.

Hence, we used tetracycline as the N source to prepare multifunctional N-Bi-O site-activated BiOBr (NBO-BiOBr) without oxygen vacancies to enhance the exciton concentration between $[\text{Bi}_2\text{O}_2]^{2+}$ slabs, and build a Z-scheme heterojunction photocatalyst with C quantum dots/ Fe_3O_4 (CQDs/ Fe_3O_4) to promote exciton dissociation. According to theoretical calculation, the exciton concentration and dissociation of BiOBr with O-Bi-OV site (OVBO-BiOBr) and NBO-BiOBr materials were analyzed. X-ray photoelectron spectroscopy (XPS), electron paramagnetic resonance (EPR), X-rays diffraction (XRD) and electron microscope were used to characterize the successful preparation of multifunctional N-Bi-O sites and heterojunction structure. Photoluminescence (PL), photoelectrochemical experiments and femtosecond time-resolved transient absorption spectroscopy (TA) showed the kinetic path of rapid exciton separation. And in situ attenuated total reflectance Fourier transform infrared (in situ ATR-FTIR) and theoretical calculations indicated that the multifunctional N-Bi-O sites were the centers of hole accumulation and TC reaction. In terms of profit, an appropriate degree of oxidation helps to produce high-value products and reduce energy waste compared to complete oxidation of pollutants. Oxidation of TC by weak holes obtained by exciton dissociation and low-oxidation-state active centers showed the highest CO evolution performance and CO selectivity, which reduced excessive oxidation.

2. Materials and methods

2.1. Chemicals and reagents

$\text{FeCl}_3 \cdot 6 \text{H}_2\text{O}$, Na_2SO_4 , citric acid monohydrate, ethylenediamine, diethylene glycol, 2,2,6,6-tetramethylpiperidine-1-oxyl (TEMPO), 5,5-dimethyl-1-pyrroline N-oxide (DMSO), $\text{Bi}(\text{NO}_3)_3 \cdot 5 \text{H}_2\text{O}$, NaH_2PO_4 , KBr, $\text{K}_3\text{Fe}(\text{CN})_6$, $\text{K}_4\text{Fe}(\text{CN})_6$, KCl, BaSO_4 , ethanol and TC. Unless stated otherwise, all the chemicals were of analytic grade (A.R.) and purchased from Sinopharm Chemical Reagent Co., Ltd. Levofloxacin hydrochloride (A.R.) was purchased from Shanghai Macklin Biochemical Co., Ltd.

2.2. Experimental procedures

2.2.1. Synthesis

2.2.1.1. Synthesis of magnetic hollow Fe_3O_4 and CQDs/ Fe_3O_4 . Experimental details were provided in [Supplementary Material](#).

2.2.1.2. Synthesis of NBO-BiOBr. Tetracycline (0.0250 g) in a three-necked flask, add ethanol (5 mL) and diethylene glycol (15 mL), and mechanically stirring until it is uniformly dissolved. Then $\text{Bi}(\text{NO}_3)_3 \cdot 5 \text{H}_2\text{O}$ (0.4851 g) and KBr (0.1190 g) to the above solution followed by mechanically stirring for a complete dispersion. The mixture was transformed into a 100 mL Teflon-lined autoclave for solvothermal reaction at 160 °C for 12 h. The resultant solid was centrifuged and washed with DI-water and ethanol. Then, the product was subjected to photocatalytic elution under visible light for 6 h, and centrifuged after the elution was completed, and the eluted product was washed with DI-water and ethanol several times. Finally, the NBO-BiOBr could be obtained by vacuum drying at 50 °C for 12 h.

2.2.1.3. Synthesis of NBO-BiOBr-HJ. Tetracycline (0.0250 g) in a three-necked flask, add ethanol (5 mL) and diethylene glycol (15 mL), and mechanically stirring until it is uniformly dissolved. Then $\text{Bi}(\text{NO}_3)_3 \cdot 5 \text{H}_2\text{O}$ (0.4851 g), KBr (0.1190 g) and CQDs/ Fe_3O_4 (0.0500 g) to the above solution followed by mechanically stirring for a complete dispersion. The mixture was transformed into a 100 mL Teflon-lined autoclave for solvothermal reaction at 160 °C for 12 h. The resultant solid was

centrifuged and washed with DI-water and ethanol. Then, the product was subjected to photocatalytic elution under visible light for 6 h, and centrifuged after the elution was completed, and the Eluted product was washed with DI-water and ethanol several times. Finally, the NBO-BiOBr-HJ could be obtained by vacuum drying at 50 °C for 12 h.

2.2.1.4. Synthesis of OVBO-BiOBr and OVBO-BiOBr-HJ. The synthesis of these two materials is in the synthesis of NBO-BiOBr and NBO-BiOBr-HJ without adding and eluting tetracycline.

2.2.2. Photocatalytic activity experiment

2.2.2.1. CO evolution performance experiment. The reaction was carried out in a closed 230 mL quartz glass reactor with circulating water. Catalysts (10 mg) and antibiotic solution (20 mL, 20 mg/L, TC) were added to the reactor. Nitrogen was bubbled into the mixture for 30 min to remove air and allow the solution to reach an equilibrium of adsorption and resolution. An LED lamp (30 W) with a wavelength of 356 nm was used as the illumination source. Every 30 min, 1 mL of gas from the quartz reactor was injected into the gas chromatography

(TetChrom, GC 2030plus) with flame ionization detector (FID) and thermal conductivity detector (TCD) for product detection.

2.2.2.2. Antibiotic removal experiment. The reaction was carried out in a closed 230 mL quartz glass reactor with circulating water. Catalysts (10 mg) and antibiotic solution (100 mL, 20 mg/L, TC) were added to the reactor. Nitrogen was bubbled into the mixture for 30 min to remove air and allow the solution to reach an equilibrium of adsorption and resolution. An LED lamp (30 W) with a wavelength of 356 nm was used as the illumination source. The absorbance of 4 mL liquid in the quartz reactor was measured by UV-vis spectrophotometer.

2.3. Other experiments and Characterizations

The photoelectrochemical properties were measured by using CHI660e electrochemical workstation. The density functional theory (DFT) calculations were calculated using the Vienna ab initio package (VASP) and CP2K package [42]. Toxicity of intermediate products evaluated by toxicity experiments and T.E.S.T. software [33]. Further experimental and characterization details were presented in the

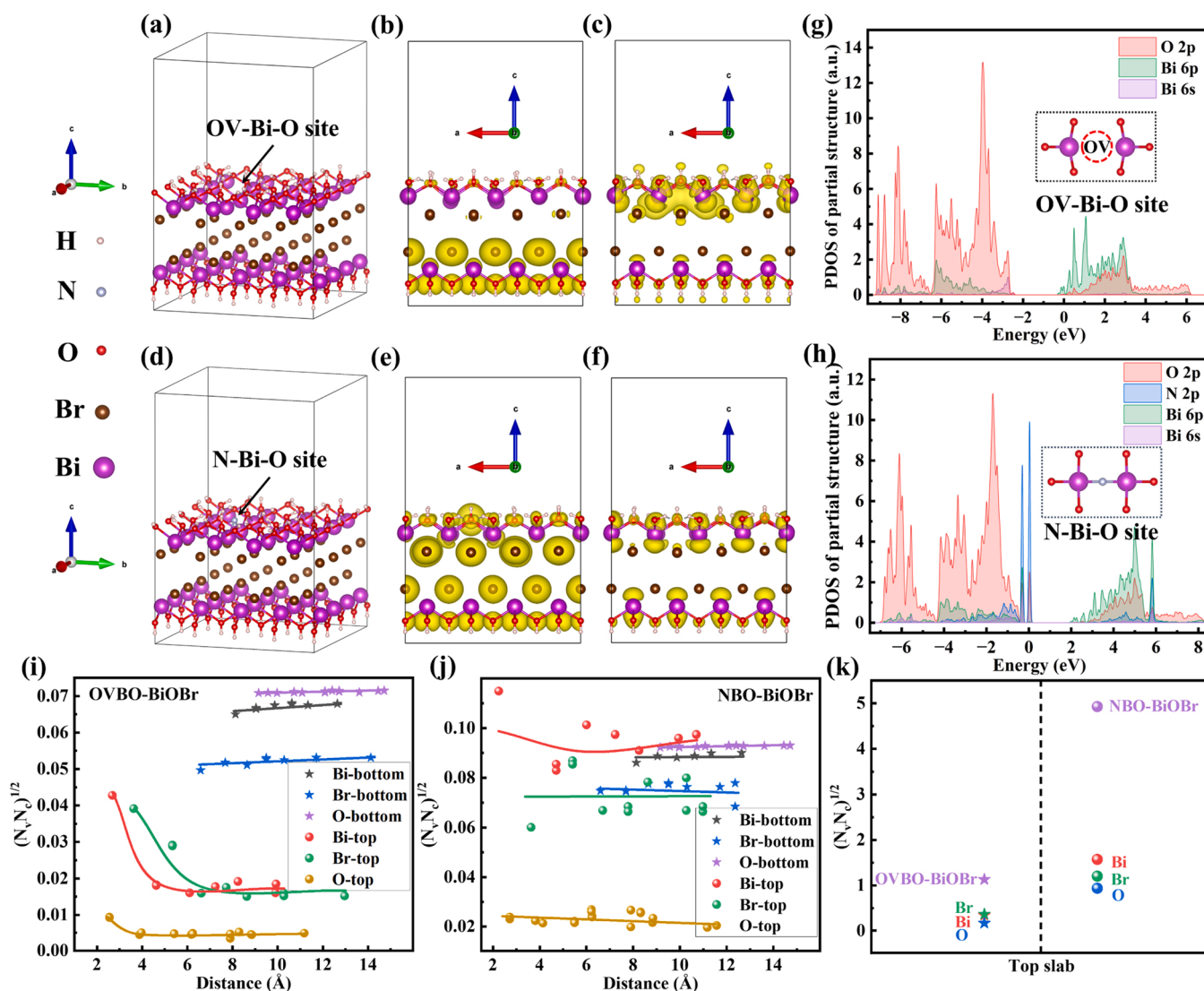


Fig. 1. (a) The optimized model, (b) valence charge density and (c) conduction charge density near the band edges of the OVBO-BiOBr. (d) The optimized model, (e) valence charge density and (f) conduction charge density near the band edges of the NBO-BiOBr. The PDOS of (g) OV-Bi-O site in OVBO-BiOBr and (h) N-Bi-O site in NBO-BiOBr. (i) $(N_c N_v)^{1/2}$ value of atomic sites at different distances around the oxygen vacancy in OVBO-BiOBr. (j) $(N_c N_v)^{1/2}$ value of atomic sites at different distances around the N atom in NBO-BiOBr. (k) $(N_c N_v)^{1/2}$ value of different elements in the top slab on OVBO-BiOBr and NBO-BiOBr.

Supplementary Material.

3. Results and discussion

3.1. Theoretical study of excitons in $[\text{Bi}_2\text{O}_2]^{2+}$ slabs

Since excitons are caused by interacting e^- and h^+ coming from the top of the valence band (VB) and the bottom of the conduction band (CB), respectively. Previous theoretical studies have focused on exciton changes in bulk BiOBr materials, and rarely on interactions between $[\text{Bi}_2\text{O}_2]^{2+}$ slabs [17,35]. Therefore, based on density functional theory (DFT), we theoretically explored the charge localization near the band-edge of low-dimensional OVBO-BiOBr and NBO-BiOBr in Fig. 1. In OVBO-BiOBr (Fig. 1a-c), the valence band-edge charge density was mainly composed of O and Br atoms at the bottom slab, while the conduction band-edge charge density was in a disordered state and mainly composed of Bi atoms at the top slab. The distribution of element electron density was similar to the reported bulk OVBO-BiOBr, but the difference of $[\text{Bi}_2\text{O}_2]^{2+}$ slab in OVBO-BiOBr was that the electron density of valence band and conduction band edge were distributed at the bottom and top of the model, respectively [35]. The existence of oxygen vacancy would not only affect the charge density localization of the surrounding Bi atom, but also change the charge density localization between $[\text{Bi}_2\text{O}_2]^{2+}$ slabs. In NBO-BiOBr (Fig. 1d-f), except that the N atom had more strong charge density at the edge of valence band, the overall exhibited a relatively uniform edge electron density, and there was no obvious difference between top and bottom. Similarly, the strength of the edge of the valence band in the partial density of state (PDOS) was illustrated in Fig. S1. After construction of N-Bi-O sites, the peak intensity and area in the red dotted box were also significantly enhanced, which intuitively echoed the charge density diagram. Further, PDOS of partial atoms around OV and N were calculated to explore the effect of orbital hybridization as shown in Fig. 1g-h. The N-Bi-O site formed a new hybrid energy level above the valence band top and promoted the mutual hybridization with N 2p, O 2p, Bi 6p and Bi 6s, significantly increasing the overall valence band electron density. However, OV-Bi-O only increased the electron density of conduction band Bi 6p, which was conducive to the rapid dissociation of excitons. Since simultaneous localization of conduction and valence band edge states is the cause of giant e^-h^+ interaction, disordered redistributed band-edge states will greatly affect the dissociation effect of excitons. Therefore, the N-Bi-O site-activated $[\text{Bi}_2\text{O}_2]^{2+}$ slabs layer attracted the Coulomb force more strongly than the oxygen vacancies, and thus the strong exciton effect.

Further, according to the work of Wang et al., the strength of the exciton effect can be expressed by the product $(N_c N_v)^{1/2}$ (N_c and N_v are the numbers of localized conduction and valence states near-gap states within a cutoff energy, respectively) of the numbers of localized valence and conduction states near the edges of different atoms [17]. In Fig. 1i-j, where the abscissa was the distance between different atoms and oxygen vacancy or N site, respectively. The $(N_c N_v)^{1/2}$ value near the oxygen vacancy in the top slab of OVBO-BiOBr was prone to form unstable small compact excitons, while the charge density at the bottom edge away from the oxygen vacancy did not change, indicating that OV-Bi-O sites would affect the charge state near by and form a charge disorder region, which was consistent with the previous report [35]. For NBO-BiOBr, there was no significant change trend in the band-edge charge density of the atoms around the N atom, indicating that N-Bi-O sites did not cause rapid exciton dissociation. It can be found that the $(N_c N_v)^{1/2}$ value of the bottom three kinds of atoms had a consistent change trend and the values were different from that of the top layer. This was because OV-Bi-O sites and N-Bi-O sites existed on the slab, and the atomic state of the bottom layer remained relatively stable. For more intuitive analysis, $(N_c N_v)^{1/2}$ value of different elements in the top slab and bottom slab was shown in Figs. 1k and S2. If the $(N_c N_v)^{1/2}$ value of the bottom atom of each material was taken as a control, it is interesting to find that the $(N_c N_v)^{1/2}$ value of the top atom of OVBO-BiOBr was significantly

reduced, while the $(N_c N_v)^{1/2}$ value of the top atom of NBO-BiOBr was basically the same. Further, whether it's at the top or the bottom, the each kind of atom in NBO-BiOBr had a higher $(N_c N_v)^{1/2}$ value than the OVBO-BiOBr. This also meant that N-Bi-O sites also led to an increase in charge density throughout the slab. Thus, stronger Coulomb interactions between e^- and h^+ were generated in N-Bi-O site-activated $[\text{Bi}_2\text{O}_2]^{2+}$ slabs layer, resulting in larger exciton binding energy, indicating a stronger exciton effect, which is logical. In order to more fully verify this problem, and to facilitate exciton dissociation and further detailed research, appropriate materials need to be constructed first.

3.2. Synthesis and characterizations of materials

In order to study the generation and dissociation of excitons in NBO-BiOBr materials, OVBO-BiOBr and OVBO-BiOBr/CQDs/ Fe_3O_4 heterojunction (OVBO-BiOBr-HJ) as control materials, NBO-BiOBr and NBO-BiOBr/CQDs/ Fe_3O_4 heterojunction (NBO-BiOBr-HJ) materials were synthesized (Figs. S3-S4). Conventional OVBO-BiOBr nanosheets stacking flower spheres were synthesized by a solvothermal method using bismuth nitrate pentahydrate and potassium bromide as precursors, and ethanol as well as diethylene glycol as solvents. Due to the existence of reducing organic compounds and the difficulty of strict control of reaction conditions, the preparation process of BiOBr often leads to defects, and forming OVBO-BiOBr [43]. And NBO-BiOBr was synthesized by a similar solvothermal method with the addition of additional TC molecules, which were decomposed by photo-elution to contribute to the formation of N-Bi-O sites due to the residual N element in TC [33]. According to thermal gravimetric analysis (TGA) (Fig. S5, Supporting Information), TC could be well present in BiOBr during synthesis. Surprisingly, this gentle approach allowed the N elements to fill in the oxygen defects around Bi atoms, blocking the formation of oxygen vacancies (See the material characterization section for more information). However, conventional N hybridization methods, such as ammonia calcination, are not only complicated and conditional, but also accompanied by the formation of a large number of oxygen vacancies (Fig. S6), resulting in a small E_b value, which affected the generation of excitons, and would form a strong electron trapping oxygen vacancy active site, which was not favorable to the oxidation process [30].

To explore the evidence of N-Bi-O sites, EPR and XPS spectrum as well as FT-IR analysis were used to collect evidence of defective structures and surface chemical bond states, respectively (Figs. 2a-e and S7). The survey XPS spectrum (Fig. S6a) indicated high purity of the samples. The Fig. 2a showed that OVBO-BiOBr samples had typical EPR signals centered on $g = 2.004$, which were determined to be oxygen vacancies capturing electrons, while NBO-BiOBr did not have any signals [44]. Similarly, XPS showed the same result signal. In Fig. 2b, the peak at the binding energy of 530.83 eV in the OVBO-BiOBr was attributed to the presence of defective oxygen, while that peak of NBO-BiOBr was absent [35]. The new added peak at 528.69 eV was attributed to the bond cooperation between the negative bivalent O and the metal Bi atom, showing a different electronic state than the conventional Bi-O bond, which might be speculated to form the N-Bi-O structure with the introduction of N [45,46]. According to Fig. S6b, the synthesis process had no effect on the Br atoms in the middle of the $[\text{Bi}_2\text{O}_2]^{2+}$ slabs layer. In Fig. 2c, the newly protrusion peaks of NBO-BiOBr without elution relative to OVBO-BiOBr at about 3400, 2969–2840 and 1114–1037 cm^{-1} corresponded to the stretching vibration of -OH bond, the stretching vibration of -CH₂- bond and the stretching vibration of C-O bond, and the red shift of Bi-O bond in fingerprint area directly indicated the new Bi-N bond [33,43]. It showed that TC and BiOBr were well combined in the process of material synthesis. After photo-elution decomposition, the almost complete disappearance of functional groups except -OH on NBO-BiOBr mean that TC was completely shed, and the peak at 527 cm^{-1} did not shift. Furthermore, in Fig. S8, the Brunauer-Emmett-Teller (BET) specific surface area was increased from 24.2579 m^2/g for OVBO-BiOBr to 37.8233 m^2/g for NBO-BiOBr in the

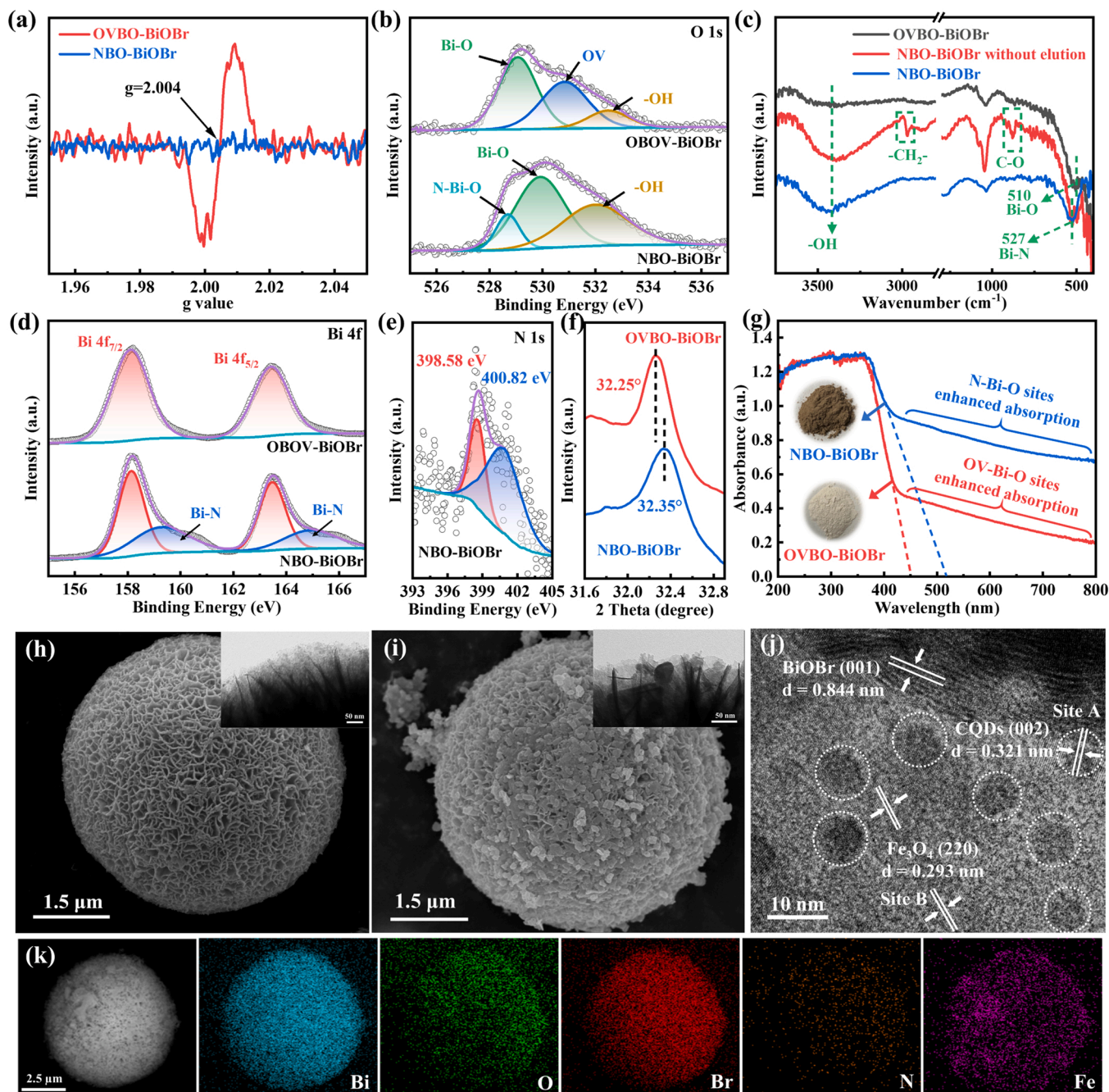


Fig. 2. (a) EPR signal. (b) High-resolution XPS spectra of O 1s (c) FT-IR spectra of OVBO-BiOBr, NBO-BiOBr without elution and NBO-BiOBr. High-resolution XPS spectra of (d) Bi 4f and (e) N 1s (f) XRD pattern of OVBO-BiOBr and NBO-BiOBr. (g) UV-vis DRS of OVBO-BiOBr and NBO-BiOBr. SEM images of (h) NBO-BiOBr and (i) NBO-BiOBr-HJ (Insert TEM images). (j) HRTEM image of NBO-BiOBr-HJ. (k) EDS mapping of NBO-BiOBr-HJ.

nitrogen adsorption-desorption experiment, which might be caused by TC detachment [47,48].

In Fig. 2d, it is worth noting that in the Bi 4f spectra of NBO-BiOBr, higher electropositive acromion (159.27 and 164.93 eV) appeared, which might indicate that Bi and N formed a bond cooperation [49,50]. In addition, the binding energy at 398.58 and 400.82 eV (Fig. 3e) appearing belonged to Bi-N bond and interstitial nitrogen or nitrogen adsorbed on the surface respectively [31,32,51–54]. The locally amplified XRD pattern of the (110) diffraction peak of NBO-BiOBr and OVBO-BiOBr were shown in Fig. 2f. NBO-BiOBr had a red shift of 0.1° for OVBO-BiOBr, which might be due to the short Bi-N bond, while oxygen defects led to wider lattice spacing, which was consistent with the results of the optimized model (Fig. S9) [55,56]. The UV-visible

diffuse reflectance spectrum (UV-vis DRS) has also been used to describe the effect of changes in the internal structure of the BiOBr on light absorption [44]. In general, pure BiOBr has no visible light absorption, and the absorption in visible light region will be enhanced after oxygen vacancies exists. Therefore, it can be seen from Fig. 2g that OVBO-BiOBr presented a light gray color. However, NBO-BiOBr without oxygen vacancies presented dark gray, which not only expanded the absorption band edge, but also has higher visible light absorption capacity, which proved that the formation of intermediate hybrid energy level promoted the reduction of band gap and contributed to the transition of photo-generated electrons. The Kubelka-Munk equation calculated the OVBO-BiOBr and NBO-BiOBr bandgaps as 2.40 and 2.17 eV, respectively (Fig. S10). In addition, the intermediate band gaps caused by

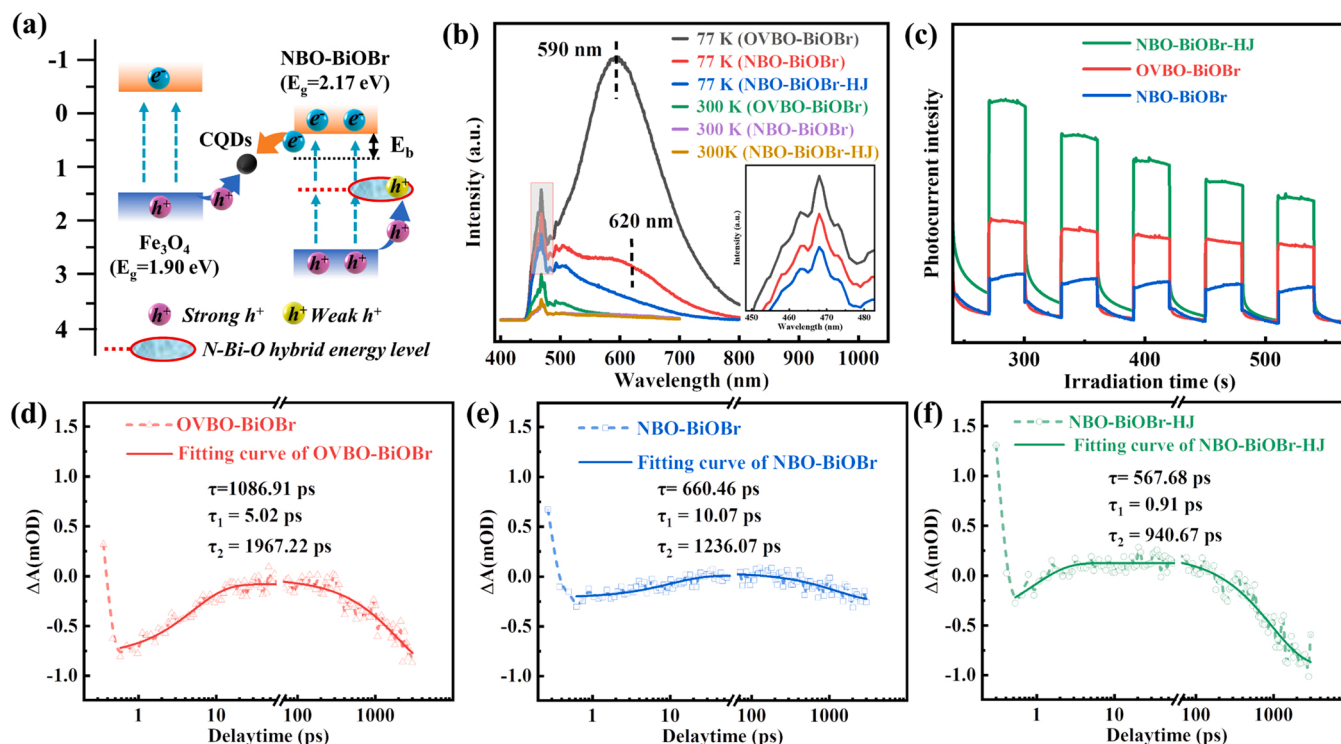


Fig. 3. (a) Z-scheme heterojunction mechanism of NBO-BiOBr-HJ. (b) Room-temperature and low-temperature fluorescence. (c) The photocurrent intensity. Transient absorption spectra kinetics at 550 nm: (d) OVBO-BiOBr, (e) NBO-BiOBr and (f) NBO-BiOBr-HJ.

OV-Bi-O sites and N-Bi-O sites were 0.34 and 0.97 eV, respectively [24]. Subsequently, the mapping spectrum in Fig. S11 also showed that the N element was uniformly distributed on the surface of NBO-BiOBr. All the evidences pointed to that TC effectively interacted with the [Bi₂O₂]²⁺ slabs during synthesis, and the N atoms substituted the oxygen defects around Bi after photo-elution decomposition, blocking the formation of oxygen vacancies.

To construct the heterojunction structure, magnetic hollow Fe₃O₄ loaded with C quantum dots (CQDs/Fe₃O₄, Figs. S12-S13) was added into the precursor solution of NBO-BiOBr to prepare NBO-BiOBr-HJ. Fe₃O₄ not only has the suitable energy level position to form heterojunction with NBO-BiOBr, but also the magnetic effect is conducive to the recycling of catalyst [57–60]. And CQDs is an excellent electron donor and acceptor, which can accelerate the interfacial band electron exchange and promote the rapid carrier migration as a composite center [61–63]. In Fig. S14, the XRD patterns of OVBO-BiOBr and NBO-BiOBr showed tetragonal crystal structure with the P4/nmm space group, which was consistent with the standard card PDF#73–2061, and no other impurity peaks were detected [35]. The (311) diffraction peak of the Fe₃O₄ with cubic structure can be clearly seen. In particular, for the synthesized heterojunction materials, the diffraction peak intensity of BiOBr was significantly decreased, which further proved that CQDs/Fe₃O₄ and NBO-BiOBr formed a good load structure. The XPS spectra of heterojunction materials was shown in Fig. S15. The XPS survey spectra of NBO-BiOBr-HJ demonstrated the Bi 4f, O 2s, Br 3d, N 1s, C 1s and Fe 2p elements, among which Bi, Br and N elements from NBO-BiOBr, while Fe signal stemmed from Fe₃O₄. For the Bi 4f spectra, the peaks at 158.32 and 163.63 eV were assigned to the Bi 4f_{7/2} and Bi 4f_{5/2}, respectively, which were Bi³⁺ of the related O elements. In addition, the other two peaks in the Bi 4f spectra at 159.74 and 165.03 eV correspond to Bi-N bond, revealing that NBO-BiOBr retained its original structure. In the O 1s spectra, the peak of oxygen vacancy at 531.30 eV still did not appear, while the peaks at 529.31 and 530.58 eV belonged to N-Bi-O, Bi-O bond, respectively, and the peaks at 528.61 and 532.31 eV belonged to Fe-O bond and -OH, respectively [58,59].

Similar to the N 1s spectra of NBO-BiOBr, Bi-N bond and interstitial nitrogen or nitrogen adsorbed on the surface were located at 398.58 and 400.03 eV, respectively. Meanwhile, the strongest peak at 283.85 eV was related to CQDs in the C 1s spectra [62]. In addition, the Fe 3p peaks for Fe₃O₄ observed at 710.26 and 723.81 eV were assigned to Fe 2p_{3/2} and Fe 2p_{1/2}, respectively [58,59].

The surface morphology and microstructure of the materials were observed by scanning electron microscopy (SEM), transmission electron microscopy (TEM) and HRTEM. In Figs. 2h and S16, both OVBO-BiOBr and NBO-BiOBr were composed of nanosheets crossed into a large flower sphere with a diameter of about 5 μm, indicating that the addition of TC did not change the morphology of BiOBr. These results demonstrated that the nanosheets composing the flower sphere were stacked. As could be seen from Fig. 2i, NBO-BiOBr still maintained the same size flower sphere morphology, and a large amount of CQDs/Fe₃O₄ was closely loaded on its surface. The BET surface areas of different materials were measured by N₂ sorption isotherm (Fig. S17). Noted that NBO-BiOBr-HJ had a larger BET surface area relative to OVBO-BiOBr-HJ and maintained the same hysteresis loop shape as NBO-BiOBr, indicating that the load of CQDs/Fe₃O₄ did not affect the physical structure of NBO-BiOBr. The uniform distribution of Fe element shown in Fig. 2k also indicated the success of the load structure. A HRTEM image revealed the crystal characteristics of NBO-BiOBr-HJ, and the position distribution between CQDs, Fe₃O₄ and NBO-BiOBr could be observed in Fig. 2j. The wide lattice fringe about 0.844 nm was the (001) crystal plane of the BiOBr, corresponding to the distance between the [Bi₂O₂]²⁺ slabs [44]. Next to it were CQDs with a diameter of about 6 nm distributed on Fe₃O₄. The lattice widths of 0.321 nm at Site A and 0.293 nm at Site B corresponded to the (002) crystal plane of CQDs and the (220) crystal plane of Fe₃O₄, respectively [60,62]. The clearer lattice stripes of the two sites were shown in Fig. S18. Therefore, the above analysis indicated that the composite structure had been successfully established.

3.3. Mechanism of exciton dissociation and carrier migration

Through UV-vis DRS, Mott-Schottky, and electron spin-resonance spectroscopy (ESR) signals of DMPO- O_2^- , it was concluded that the composite was constructed into Z-scheme heterojunction, which was shown in Figs. 3a and S19-21 [64,65]. After photoexcitation, due to the existence of large exciton binding energy in N-Bi-O site-activated $[\text{Bi}_2\text{O}_2]^{2+}$ slabs, the reduction potential of exciton-dissociated e^- was reduced, and then the e^- were easily transferred to CQDs and recombined with the h^+ from Fe_3O_4 . Since the hybrid energy level formed by N-Bi-O sites was about 1.19 eV higher than the top of the valence band, the strong holes in the valence band were easy to transfer to this low-oxidation-state energy level, and thus the weak holes were formed.

Both N-Bi-O sites and heterogeneous structure construction can affect the migration and utilization of charge carrier and thus affect exciton generation and dissociation efficiency; hence, several photoelectrochemical experiments were conducted to investigate. The results of electrochemical impedance spectroscopy (EIS) (Fig. S22) showed that the heterojunction blocked the e^- transport in OVBO-BiOBr, and the NBO-BiOBr-HJ heterojunction structure provided a good e^- transfer channel. Furthermore, photoluminescence (PL) spectroscopy was used to record the exciton effect in the different materials in Fig. 3b. At room temperature (300 K), the fluorescence intensity at 468 nm corresponded to the intrinsic band-edge emission of BiOBr [66]. The OVBO-BiOBr had high fluorescence intensity, while NBO-BiOBr and NBO-BiOBr-HJ had low fluorescence intensity because NBO-BiOBr materials had indirect band gap characteristics [35]. Time-resolved PL decay spectra (Fig. S23) monitored at the corresponding steady-state emission peaks yield mean radiative lifetimes of 1.70, 1.41 and 0.79 ns for OVBO-BiOBr, NBO-BiOBr and NBO-BiOBr-HJ, respectively. Compared with OVBO-BiOBr, the existence of strong exciton binding in NBO-BiOBr could shorten the fluorescence lifetime and reduce the carrier lifetime, while the shortening of fluorescence lifetime in NBO-BiOBr-HJ was due to the formation of electronic channels to accelerate the exciton separation. The dark characteristics and non-radiative relaxation of excitons could be better captured at low temperature, and the fluorescence spectra of the BiOBr materials were recorded at a low temperature of 77 K. In Fig. 3b, the eigen peaks were enhanced at low temperatures due to singlet exciton recombination. The fluorescence intensity of NBO-BiOBr-HJ was lower than that of NBO-BiOBr, indicating that the construction of heterojunction promoted the dissociation of exciton. In addition, the OVBO-BiOBr showed another distinct emission peak at approximately 570 nm, which could be correlated with the OV-Bi-O state [35]. The NBO-BiOBr emission peak at approximately 610 nm, which was correlated with the N-Bi-O state, and indicated that the N-Bi-O hybrid energy level did not act as strong recombination centers for electrons. The photocurrent recording of carrier migration inside the different materials were shown in Fig. 3c. The NBO-BiOBr had low photocurrent intensity, while OVBO-BiOBr had O-Bi-OV sites promoting exciton separation, which was consistent with the literature reports [35]. It was worth noting that the construction of NBO-BiOBr for suitable heterojunction could accelerate carrier migration, which might be related to the rapid exciton separation.

To further explain the exciton formation and dissociation states in different materials, the electron transfer dynamics were studied in detail using TA spectroscopy [67–69]. It was worth noting that the excitation wavelength and content of BiOBr were different from those of Fe_3O_4 and CQDs, and all the signals in the detection window belonged to BiOBr signals. Fig. S24 described the representative TA spectra at 0.36 ps delay to understand exciton generation. The probe bleach signal in the light green region (about 425 nm) might be related to neutral singlet excitons caused by photogenerated e^- and h^+ [70]. Noted that NBO-BiOBr was significantly stronger than OVBO-BiOBr. Conversely, the positive signal in the light blue region (525–575 nm) was associated with free charge carriers, where NBO-BiOBr was weaker than OVBO-BiOBr [35]. Therefore, due to the strong exciton effect and the higher charge density

caused by N-Bi-O sites, the N-Bi-O site-activated $[\text{Bi}_2\text{O}_2]^{2+}$ slabs would generate a large number of photogenerated e^- and h^+ to induce excitons. Due to exciton effect, photoexcited electron-hole pairs can promote the formation of triplet excitons through an intersystem crossing, and further activate triplet O_2 ($^3\Sigma_g^-$) easily through excitonic energy transfer to produce singlet oxygen ($^1\text{O}_2$, $^1\Delta_g$) [36]. Therefore, it was also proved that NBO-BiOBr had stronger exciton effect by detecting TEMP- $^1\text{O}_2$ signals (Fig. S25). In Fig. S26, detailed TA spectra of different samples were shown. The three samples showed the same signal detection trend. First of all, the ground-state bleach (GSB) signal features dominated. The strongest bleaching signal of OVBO-BiOBr might be caused by OV-Bi-O sites, while the weak bleaching signal of NBO-BiOBr and NBO-BiOBr-HJ was caused by N-Bi-O sites [71,72]. The GSB signal first attenuated about 20 ps and then strengthened for a long time. The trend of signal detection was more comprehensively shown in the heatmap (Fig. S27) under multi-wavelength conditions.

Accordingly, the kinetic decay signals at 550 nm were taken, and the optimal multi-exponential function fitting parameters were listed in Fig. 3d-f and Table S1. The fast decay time τ_1 was concentrated in a few picoseconds, which could be attributed to the migration of photoexcited e^- from the bottom of the conduction band to the exciton-mediate trap state. The decay time τ_1 (10.07 ps) of NBO-BiOBr was higher than that of OVBO-BiOBr (5.02 ps), which was related to the generation of a large number of excitons in NBO-BiOBr and the promotion effect of rapid exciton dissociation in OVBO-BiOBr. It was worth noting that the decay time τ_1 of NBO-BiOBr-HJ was shortened to a very small (0.91 ps). Different from NBO-BiOBr, the construction of heterostructure effectively promoted the rapid dissociation effect of excitons, and thus increase the rate of exciton generation. As the delay time increased, the bleaching signal began to gradually increase and the e^- were further captured. The deep trap defects and oxygen defects in OVBO-BiOBr would trap e^- effectively and decay time τ_2 reached 1967.22 ps. However, the lack of deep trap defects in NBO-BiOBr would decay more rapidly (1236.0 ps), and the decay intensity of bleaching signal was much lower than that of OVBO-BiOBr, leading to the rapid recombination of carrier. This also suggested that the N-Bi-O hybrid energy level formed was not a suitable center for electron capture. According to similar reports, the decay time τ_2 (940.6 ps) of NBO-BiOBr-HJ was caused by the extra e^- capture state, the e^- on NBO-BiOBr were transferred through the Z-scheme heterostructure, and the h^+ from Fe_3O_4 were rapidly recombined on CQDs [35]. The average electron transfer time of OVBO-BiOBr, NBO-BiOBr and NBO-BiOBr-HJ was 1086.98 ps, 660.46 ps and 567.68 ps, respectively. The long electron transfer time of single materials was more conducive to the long life of carriers, while the fast electron separation time of heterojunction materials was more conducive to the generation of long-life holes. Therefore, N-Bi-O site-activated $[\text{Bi}_2\text{O}_2]^{2+}$ slabs structural in NBO-BiOBr could effectively increase exciton generation, while the construction of NBO-BiOBr-HJ heterojunction could effectively dissociate excitons to produce many free holes, and the holes were further transferred to the higher N-Bi-O hybrid energy level to form weak holes.

3.4. Proof of N-Bi-O sites as selective active centers

A good active center plays an important role in the efficiency of the catalytic conversion reaction, which requires that the reaction site not only has a good adsorption capacity, but also can enrich holes. Previous studies have shown that adding target pollutant molecules (TC in this work) into the synthesis process can construct selective recognition sites for target pollutant molecules on the catalyst surface to improve the selective photocatalytic performance [33]. Therefore, the recognition and hole transfer mechanism of the different materials on TC was proved by in situ ATR-FTIR and DFT calculations.

In Fig. S28, the difference charge density of NBO-BiOBr showed that N-Bi-O site could effectively enrich electrons and affect the charge distribution around it. The electron gain and loss of the top slab atom was

clearly shown by the Bard charge analysis. The N atom obtained 0.82 electron, which was higher than its surrounding O atoms, and also improved the partial enrichment of electrons on its surrounding Bi atoms. This theoretically indicated that N-Bi-O sites had the potential as active centers. Subsequently, in situ ATR-FTIR was also implemented to prove this point. In Fig. 4a-b, compared with OVBO-BiOBr, NBO-BiOBr had some additional absorption peaks for TC adsorption. Furthermore, the peaks from 2900 to 2800 cm^{-1} correspond to the tensile vibration of $-\text{CH}_2-$, while the peaks from 1550 to 1500 cm^{-1} belong to C-N and N-H, indicating that the N atoms in N-Bi-O sites were easy to interact with the methyl carbon in TC [33]. Therefore, the adsorption between methyl group in TC and NBO-BiOBr surface was constructed. The absorption peak intensity of OVBO-BiOBr did not change significantly in 60 min, indicating that the OV-Ni-O sites effect were less than that of N-Bi-O sites. After absorbing TC from OVBO-BiOBr and NBO-BiOBr materials

for 30 min, the powders were dried and FT-IR tests were conducted. In Fig. S29, it was found that NBO-BiOBr showed stronger absorption peak of TC adsorption. Furthermore, ATR-FTIR spectra of 4000–2750 cm^{-1} were displayed in Fig. S30. In the TC adsorption process of the two materials, the peak strength of $-\text{OH}$ group were negative, which was because the adsorption of TC would lead to the unstable $-\text{OH}$ group shedding on the material surface. Therefore, it is reasonable to assume that the $-\text{OH}$ group on the material surface did not participate in the TC adsorption process. The growth peak at about 3500 cm^{-1} was referred to as the N-H bond, which was related to the adsorption of TC by NBO-BiOBr. Theoretical calculations were also used to further demonstrate the superiority of N-Bi-O sites (Fig. 4c-d and Table S2). The adsorption energy of NBO-BiOBr (-5.470 eV) on TC was higher than that of OVBO-BiOBr (-1.553 eV), and the electron interaction was stronger, indicating that the N atoms in N-Bi-O sites could effectively

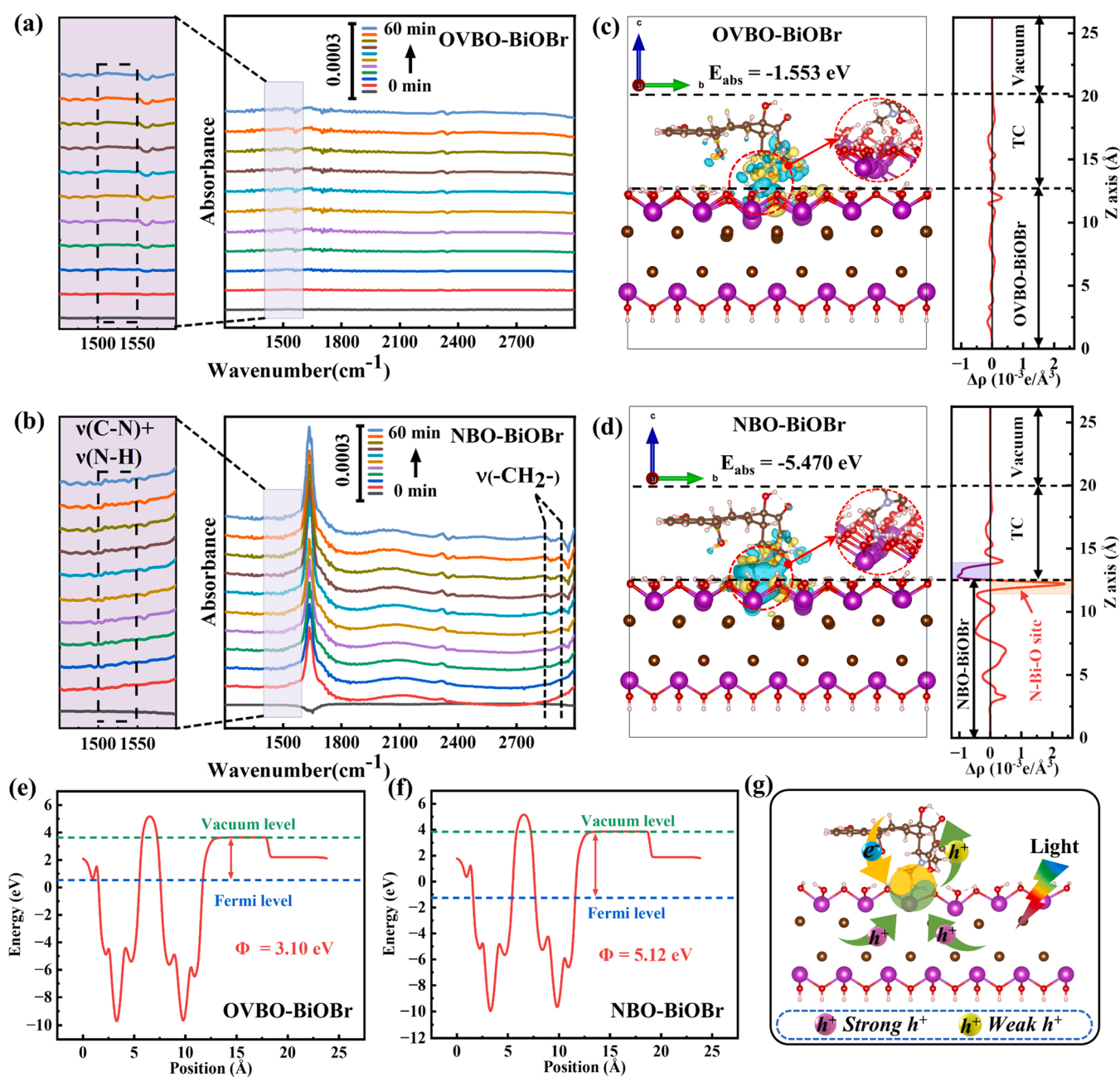


Fig. 4. In situ ATR-FTIR spectra of adsorption for TC on (a) OVBO-BiOBr and (b) NBO-BiOBr. The planar-averaged electron density difference and adsorption energy of adsorption for TC on (c) OVBO-BiOBr and (d) NBO-BiOBr. The work function of (e) OVBO-BiOBr and (f) NBO-BiOBr. (g) Schematic diagram of TC adsorption mechanism and holes enrichment in low-oxidation-state active centers. (Bi: purple, O: red, Br: dark gray, C: light gray, N: light blue and H: white).

adsorb TC and improve the interaction between TC and BiOBr surface. At the same time, TC and NBO-BiOBr formed new C-N and N-H bonds in the optimized structure, while TC was mainly electrostatic interaction with OVBO-BiOBr. To further demonstrate the selectivity of NBO-BiOBr for TC adsorption, LEV (an antibiotic with a different structure from TC) was used as the control pollutant for selective photocatalytic experiments (Fig. S31 and Table S3), which showed that NBO-BiOBr had the advantage of selective photocatalysis for TC.

In addition, the active centers also play an important role in the enrichment of holes during photoconversion. Fig. 4e-f showed the work function (Φ) analysis of OVBO-BiOBr and NBO-BiOBr, and this parameter represented the electron enrichment capacity of the material [1,73]. The work function of NBO-BiOBr was 5.12 eV, which was higher than that of OVBO-BiOBr (3.10 eV), indicating that the surface of NBO-BiOBr had a stronger ability to capture electrons. This conclusion was consistent with the trend of work function calculated by ultraviolet photoelectron spectra (UPS) in Fig. S32 [74]. Echoing Fig. 4c-d, the electrons on TC were transferred to the N atoms in N-Bi-O sites, and the number of electrons was significantly higher than that of OV-Bi-O sites, which might be caused by the formation of C-N bond to promote the transfer of

carrier. In combination with the above analysis, the low-oxidation-state active centers were filled with a large number of electrons and has a strong attraction force to holes [75]. After light exposure, a large number of holes can be accumulated in this active center. Due to the consumption between electrons and holes as well as the high N-Bi-O hybrid energy level, the strong holes generated by the valence band would be transformed into weak holes, so low-oxidation-state active centers would be formed [16,24–26]. Schematic diagram of TC adsorption mechanism and holes enrichment in low-oxidation-state active centers was shown in Fig. 4g. Specifically, TC would migrate to the low-oxidation-state active centers and further inject electrons. At this time, strong holes after exciton dissociation would be attracted to the low-oxidation-state active centers to form a large number of weak holes, which led to a short migration path of weak holes and could quickly realize the attack on TC. According to the results of selective photocatalytic experiments (Fig. S31 and Table S3), the more prominent selective photocatalytic performance of TC after the construction of heterojunction was caused by the formation of a large number of weak holes. Therefore, the low-oxidation-state active centers constructed by N-Bi-O sites can effectively selectively adsorb and catalyze TC. In

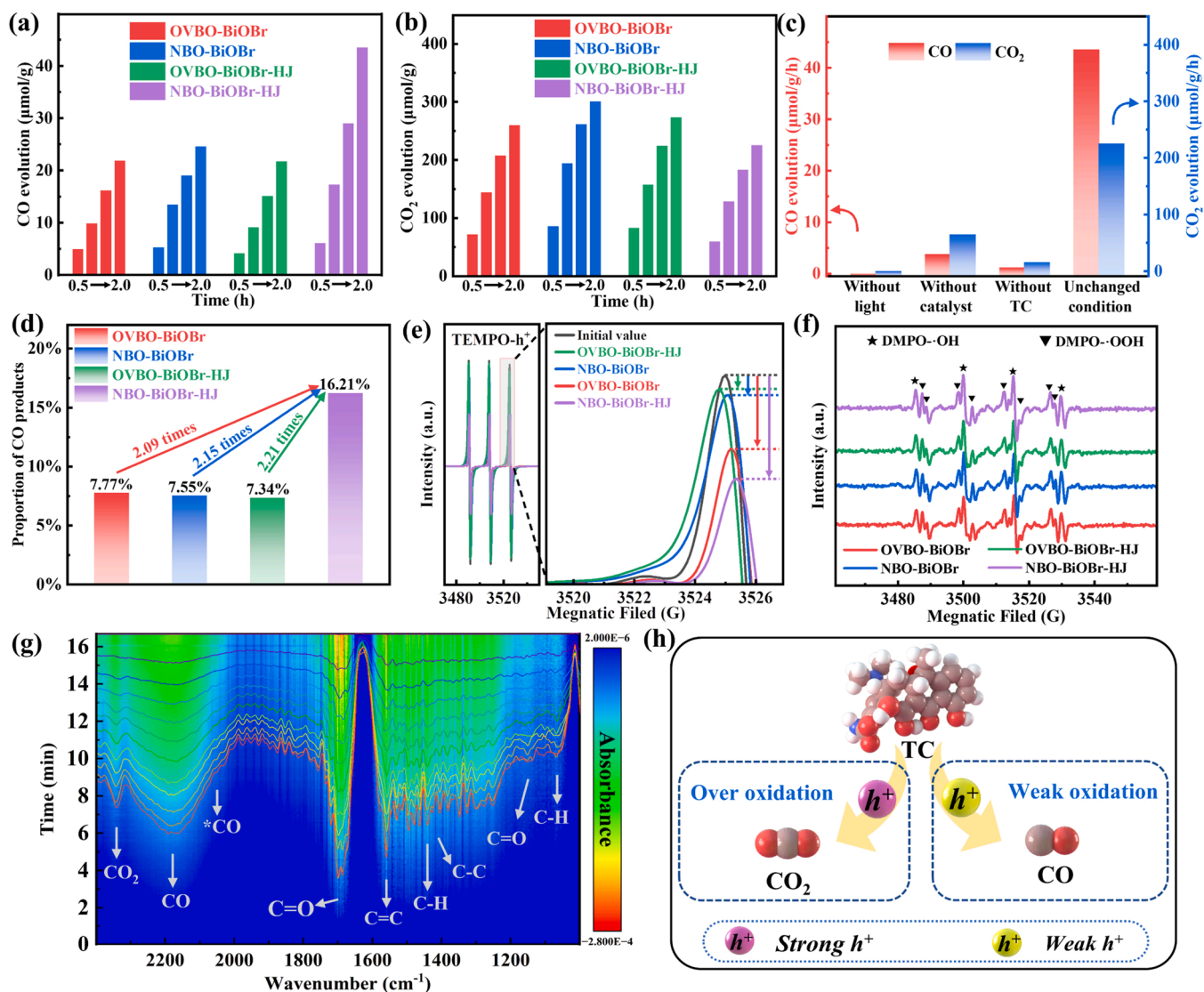


Fig. 5. Photoconversion of TC into (a) CO and (b) CO₂ evolution over different photocatalysts. (c) Photoconversion of TC into CO evolution performance of NBO-BiOBr-HJ under different conditions. (d) The ratio of CO yield to CO₂ yield. ESR spectra of (e) TEMPO trapped h^+ radicals and (f) DMOP trapped radicals in water solution with the light irradiation for 20 min (g) *In situ* ATR-FTIR study of TC with NBO-BiOBr-HJ at different time intervals under illumination. (h) Schematic diagram of TC molecule being oxidized by holes with different intensities of oxidation. (O: red, C: light gray, N: blue and H: white).

addition, for pollutants, researchers usually completely oxidize them to achieve the purpose of removal, ignoring that the control of oxidation degree can cause feedstocks to form different intermediate products [2, 8,76]. Here the weak holes generated from the low-oxidation-state active centers may prevent excessive oxidation of pollutants resulting in the formation of high value products.

3.5. Photocatalytic selective conversion of TC into CO performance

The influence of weak holes produced by low-oxidation-state active centers on the types of converted products were further explored. In Fig. 5a, the photoconversion of TC into CO evolution performance for a series of materials was shown. In the photoconversion TC experiment, the CO evolution rates of OVBO-BiOBr and NBO-BiOBr under 2 h illumination were 21.84 and 24.56 $\mu\text{mol/g}$, respectively. Notably, the performance of NBO-BiOBr-HJ was improved to 43.53 $\mu\text{mol/g}$, which was higher than that of the single materials and OVBO-BiOBr-HJ. For CO_2 (Fig. 5b), the photoconversion of TC into CO_2 by OVBO-BiOBr, NBO-BiOBr, OVBO-BiOBr-HJ and NBO-BiOBr-HJ under 2 h illumination was 259.38, 300.53, 273.58 and 225.23 $\mu\text{mol/g}$, respectively. Using other pollutants (LEV, methylene blue and p-nitrotoluene) as feedstocks could also be photoconverted into CO (Fig. S33). In addition, the selective conversion effect of N-Bi-O sites on TC was also demonstrated by comparing the performance of LEV photoconversion into CO using different materials (Fig. S34). In Fig. S35-37, the solution after TC reaction was detected by mass spectrometry (MS), and the toxicity of the intermediate products was gradually reduced by path prediction and theoretical toxicity analysis. To investigate the sources of CO and CO_2 , a series of performance tests for NBO-BiOBr-HJ were carried out (without light, catalyst or TC), and results were shown in Fig. 5c. In the absence of light, no gas was produced, suggesting that light was the source of energy that drives the whole reaction. Meanwhile, TC would also produce a small amount of decomposition in pure water, which might be related to the relatively strong photostability of TC [27]. In the absence of TC, no gas products were produced. It could be concluded that CO and CO_2 were converted from carbon element in TC. Subsequently, the stability of the material was tested for seven times, which was shown in Fig. S38a. The CO evolution performance decreased slightly, but still maintaining 37.00 $\mu\text{mol/g/h}$. In Fig. S38b-c, it also showed good magnetic recyclability and stability, indicating that the material had good reusability.

The proportion of CO products was used to represent the effect of selective CO evolution and was shown in Fig. 5d. The proportion of reducing TC to CO by NBO-BiOBr-HJ was 16.21%, more than twice that of other three materials. Meanwhile, carbon conversion performance (Molar percentage of carbon content in high-value products to carbon content in feedstocks) for photoconversion of NBO-BiOBr-HJ reached 1.10% per hour, higher than some current reports, such as CO_2 conversion, plastic conversion and biomass conversion (Table S4). In order to explore the main active groups of photoconversion TC, electron spin-resonance spectroscopy (ESR) experiments were performed. The holes signal intensity was detected using 2,2,6,6-tetramethylpiperidine-1-oxyl (TEMPO) as capture agent. In Fig. 5e, OVBO-BiOBr had a lower intensity signal than NBO-BiOBr and generated more holes, which might be related to the oxygen vacancy that was conducive to exciton separation. After the heterojunction was constructed, the signal of OVBO-BiOBr-HJ was increased, which was because the construction of heterojunction was not conducive to the separation of carriers in OVBO-BiOBr, while the signal strength of NBO-BiOBr-HJ reached the lowest level, indicating that more exciton-dissociated h^+ were generated. As mentioned above, the exciton-dissociated h^+ were more likely to migrate to the low-oxidation-state active centers to form weak holes. The intensity of ESR signals (Fig. 5f) captured by 5,5-dimethyl-1-pyrroline N-oxide (DMSO) were basically the same in all materials. Therefore, it was concluded that OH and OOH played an insignificant role in the photoconversion of TC into CO, while the weak holes produced in the low-oxidation-state active centers played a major role. In order to exclude electron

reduction, silver nitrate was added in the experiment as an electron trapping agent (Fig. S39). The performance of all materials for CO evolution from TC was improved. This was further evidence that the CO formed by the direct oxidation of TC by the holes.

To understand the chemical functionality of organic species during the conversion photocatalytic reaction of TC, an in situ ATR-FTIR study was performed under illumination (Fig. 5g). The absorption peaks at 1691 and 1142 cm^{-1} were assigned to carbonyl group ($\text{C}=\text{O}$), which might be related to keto group in TC [77]. A peak at 1558 cm^{-1} was stretching of the $\text{C}=\text{C}$ bond, and the band that appeared at 1411 cm^{-1} was due to a stretching of the $\text{C}-\text{C}$ bond [33,77]. These two peaks were assigned to the cyclic carbonyl compounds. The absorption peak at 1437 cm^{-1} corresponded to the bend of $\text{C}-\text{H}$, while the peak at 1066 cm^{-1} was due to $\text{C}-\text{H}$ deformation and stretching vibration of in ring structure [33,77,78]. Previous studies have shown that $\text{C}=\text{O}$ bond and the stretching of $\text{C}-\text{H}$ bond facilitate CO formation in catalytic conversion systems [77]. The peaks at 2174 and 2057 cm^{-1} were observed, which were referred to as the formation of CO molecule and $^*\text{CO}$ intermediate during the catalytic process, respectively [78,79]. The band that appeared at 2343 cm^{-1} was due to the formation of CO_2 , one of the most important products of oxidation of organic compounds [77]. Thus, the disintegration of these bonds indicated that NBO-BiOBr-HJ could accelerate the bond cleavage of TC and produce CO under light conditions. Hence, schematic diagram of TC molecule being oxidized by holes with different intensities of oxidation showed in Fig. 5h. A large number of weak holes in NBO-BiOBr-HJ after exciton dissociation tend to oxidize TC molecules into CO, while the photogenerated strong holes formed by other materials are not only small in number, but also strong in oxidation, which can deeply oxidize TC molecules into CO_2 .

Based on the above analysis, we proposed a possible mechanism of photoconversion of TC into CO on NBO-BiOBr-HJ under light conditions in Fig. 6. NBO-BiOBr was photoexcited to produce photogenerated electrons and holes. Due to the increase of local electron density at the edge of valence band caused by N-Bi-O sites, the Coulomb force in $[\text{Bi}_2\text{O}_2]^{2+}$ slabs formed excitons and further promoted the photoexcitation process, which led to the increase of exciton concentration. At the same time, the electronic fast recombination channel in heterojunction promoted the rapid transfer of bound electrons in excitons. This behavior rapidly dissociated excitons and produced a large number of free strong holes which were quickly transferred to the low-oxidation-state active centers composed of multifunctional N-Bi-O sites. Since the higher holes energy level position and charge attraction at this active center, the strong holes transformed into weak holes with lower energy. Importantly, the low-oxidation-state active center was also the main TC reaction site. Promoting weak holes were more likely to directly attack TC and more inclined to produce CO rather than over oxidation.

4. Conclusion

In conclusion, an oxygen defect-free N-Bi-O site-activated BiOBr with TC as nitrogen source was prepared, and a Z-scheme heterojunction photocatalyst was constructed by loading CQDs/ Fe_3O_4 on its surface. The generation and rapid dissociation of excitons and the formation of a large number of free holes were facilitated by the reasonable construction of N-Bi-O sites and heterojunction, and a new low-oxidation-state active center was also created. Interestingly, the low-oxidation-state active center can not only enrich the holes and reduce the oxidation capacity of the dissociated holes, but also acted as the main reactive site of TC, which directly led to weak holes attacking TC directly and preventing excessive reaction. As a result, the yield of TC into CO by photoconversion of NBO-BiOBr-HJ was 43.53 $\mu\text{mol/g}$, the proportion of CO products was 16.21%, which was 2.2 times of that of other reference materials, and the 2 h carbon conversion rate reached 2.20%. This work might bring new insights into the reasonable modification of photocatalyst to construct proper holes in photoconversion systems.

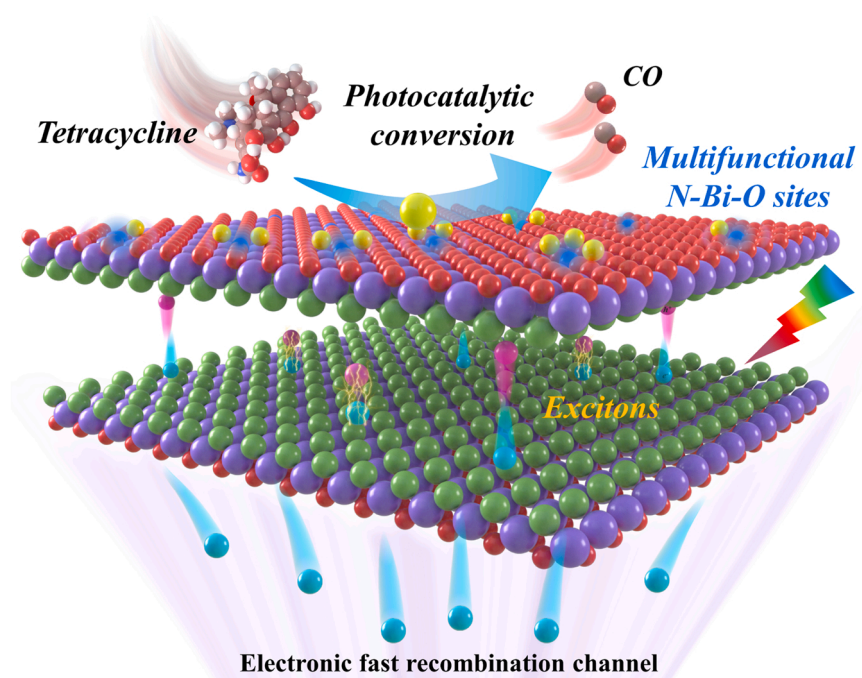


Fig. 6. Possible mechanism of photoconversion of TC into CO on NBO-BiOBr-HJ. (Bi: purple, O: red, Br: dark gray, C: light gray, N: light blue, H: white, electron: blue, weak hole: yellow and strong hole: pink).

CRediT authorship contribution statement

Guosheng Zhou: Methodology, Validation, Data curation, Writing – original draft. **Yangrui Xu:** Writing – original draft, Data curation. **Yu Cheng:** Writing – review & editing, Data curation. **Zehui Yu:** Methodology, Data curation. **Binghui Wei:** Validation. **Xinlin Liu:** Methodology, Resources, Project administration. **Ziran Chen:** Software. **Chunxiang Li:** Investigation, Resources. **Ziyang Lu:** Conceptualization, Resources, Writing – review & editing, Supervision.

Declaration of Competing Interest

The authors declare that they have no known competing financial interests or personal relationships that could have appeared to influence the work reported in this paper.

Data availability

Data will be made available on request.

Acknowledgements

This work was supported by the National Natural Science Foundation of China (22278190), China Postdoctoral Science Foundation (2022M711382), Zhenjiang Carbon Emissions Peak/Carbon Neutrality Science and Technology Innovation Special Fund Project (CQ2022009), Young Scientific and Technological Talents Support Project of Jiangsu Association for Science and Technology, Open Project of State Key Laboratory of Structural Chemistry (20230022), Jiangsu Collaborative Innovation Center of Technology and Material of Water Treatment, Project of Research on Educational Reform and Talent Development, School of Emergency Management, Jiangsu University (JG-03-11), and the Special Scientific Research Project of School of Emergency Management, Jiangsu University (KY-C-12).

Appendix A. Supporting information

Supplementary data associated with this article can be found in the online version at [doi:10.1016/j.apcatb.2023.122892](https://doi.org/10.1016/j.apcatb.2023.122892).

References

- [1] H. Zhou, M. Wang, F. Wang, Oxygen-controlled photo-reforming of biopolyols to CO over Z-scheme CdS@g-C₃N₄, *Chem* 8 (2022) 465–479.
- [2] J. Xu, X. Jiao, K. Zheng, W. Shao, S. Zhu, X. Li, J. Zhu, Y. Pan, Y. Sun, Y. Xie, Plastics-to-syngas photocatalysed by Co-Ga₂O₃ nanosheets, *Natl. Sci. Rev.* 9 (2022) nwac011.
- [3] Z. Lu, F. He, C.Y. Hsieh, X. Wu, M. Song, X. Liu, Y. Liu, S. Yuan, H. Dong, S. Han, Magnetic hierarchical photocatalytic nanoreactors: toward highly selective Cd²⁺ removal with secondary pollution free tetracycline degradation, *ACS Appl. Nano Mater.* 2 (2019) 1664–1674.
- [4] Z. Zhang, X. Huang, B. Zhang, Y. Bi, High-performance and stable BiVO₄ photoanodes for solar water splitting via phosphorus-oxygen bonded FeNi catalysts, *Energy Environ. Sci.* 15 (2022) 2867–2873.
- [5] Y.R. Xu, X.D. Zhu, H. Yan, P.P. Wang, M.S. Song, C.C. Ma, Z.R. Chen, J.Y. Chu, X. L. Liu, Z.Y. Lu, Hydrochloric acid-mediated synthesis of ZnFe₂O₄ small particle decorated one-dimensional Perylene Diimide S-scheme heterojunction with excellent photocatalytic ability, *Chin. J. Catal.* 43 (2022) 1111–1122.
- [6] C. Dong, Y. Yang, X. Hu, Y. Cho, G. Jang, Y. Ao, L. Wang, J. Shen, J.H. Park, K. Zhang, Self-cycled photo-Fenton-like system based on an artificial leaf with a solar-to-H₂O₂ conversion efficiency of 1.46, *Nat. Commun.* 13 (2022) 4982.
- [7] S.S. GC, K. Alkanad, B. Thejaswini, G. Alnaggar, N. Al Zaqri, Q. Drmash, A. Boshala, N. Lokanath, Alkaline mediated sono-synthesis of surface oxygen-vacancies-rich cerium oxide for efficient photocatalytic CO₂ reduction to methanol, *Surf. Interfaces* 34 (2022), 102389.
- [8] X. Jiao, K. Zheng, Q. Chen, X. Li, Y. Li, W. Shao, J. Xu, J. Zhu, Y. Pan, Y. Sun, Y. Xie, Photocatalytic Conversion of Waste Plastics into C(2) Fuels under Simulated Natural Environment Conditions, *Angew. Chem., Int. Ed.* 59 (2020) 15497–15501.
- [9] M. Ran, H. Xu, Y. Bao, Y. Zhang, J. Zhang, M. Xing, Selective production of CO from organic pollutants by coupling piezocatalysis and advanced oxidation processes, *Angew. Chem., Int. Ed.* (2023), e202303728.
- [10] Y. Ren, G. Zhou, Z. Lu, Utilization of porous liquids for catalytic conversion, *Chin. J. Struct. Chem.* (2023), 100045.
- [11] X. Jiao, Z. Hu, K. Zheng, J. Zhu, Y. Wu, X. Zhang, J. Hu, W. Yan, J. Zhu, Y. Sun, Y. Xie, Direct polyethylene photoreforming into exclusive liquid fuel over charge-asymmetrical dual sites under mild conditions, *Nano Lett.* 22 (2022) 10066–10072.
- [12] H. Che, X. Gao, J. Chen, J. Hou, Y. Ao, P. Wang, Iodide-Induced Fragmentation of Polymerized Hydrophilic Carbon Nitride for High-Performance Quasi-Homogeneous Photocatalytic H₂O₂ Production, *Angew. Chem., Int. Ed.* 60 (2021) 25546–25550.

- [13] S. Huang, T. Ouyang, B.F. Zheng, M. Dan, Z.Q. Liu, Enhanced Photoelectrocatalytic Activities for CH₃OH-to-HCHO Conversion on Fe₂O₃/MoO₃: Fe-O-Mo Covalency Dominates the Intrinsic Activity, *Angew. Chem., Int. Ed.* 60 (2021) 9546–9552.
- [14] C. Yang, S. Wan, B. Zhu, J. Yu, S. Cao, Calcination-regulated Microstructures of Donor-Acceptor Polymers towards Enhanced and Stable Photocatalytic H₂O₂ Production in Pure Water, *Angew. Chem., Int. Ed.* 61 (2022), e202208438.
- [15] S. Huang, F. Feng, R.T. Huang, T. Ouyang, J. Liu, Z.Q. Liu, Activating C-H Bonds by Tuning Fe Sites and an Interfacial Effect for Enhanced Methanol Oxidation, *Adv. Mater.* 34 (2022), e2208438.
- [16] B. Qiu, L. Cai, N. Zhang, X. Tao, Y. Chai, A Ternary, Dumbbell structure with spatially separated catalytic sites for photocatalytic overall water splitting, *Adv. Sci.* 7 (2020) 1903568.
- [17] H. Wang, S. Chen, D. Yong, X. Zhang, S. Li, W. Shao, X. Sun, B. Pan, Y. Xie, Giant electron-hole interactions in confined layered structures for molecular oxygen activation, *J. Am. Chem. Soc.* 139 (2017) 4737–4742.
- [18] H. Wang, S. Jin, A. Wang, X. Jiang, W. Liu, X. Zhang, W. Yan, K. Yu, J. Zhao, Y. Xie, Engineering exciton-phonon interactions for suppressing nonradiative energy loss in energy-transfer-initiated photocatalysis, *CCS Chem.* 5 (2023) 234–244.
- [19] H. Wang, W. Liu, X. He, P. Zhang, X. Zhang, Y. Xie, An excitonic perspective on low-dimensional semiconductors for photocatalysis, *J. Am. Chem. Soc.* 142 (2020) 14007–14022.
- [20] Q. Guo, Y. Liu, M. Liu, H. Zhang, X. Qian, J. Yang, J. Wang, W. Xue, Q. Zhao, X. Xu, W. Ma, Z. Tang, Y. Li, Z. Bo, Enhancing the performance of organic solar cells by prolonging the lifetime of photogenerated excitons, *Adv. Mater.* 32 (2020), e2003164.
- [21] Y. Li, H. Wang, X. Zhang, S. Wang, S. Jin, X. Xu, W. Liu, Z. Zhao, Y. Xie, Exciton-mediated energy transfer in heterojunction enables infrared light photocatalysis, *Angew. Chem., Int. Ed.* 60 (2021) 12891–12896.
- [22] W. Zhang, C. Fu, J. Low, D. Duan, J. Ma, W. Jiang, Y. Chen, H. Liu, Z. Qi, R. Long, Y. Yao, X. Li, H. Zhang, Z. Liu, J. Yang, Z. Zou, Y. Xiong, High-performance photocatalytic nonoxidative conversion of methane to ethane and hydrogen by heteroatoms-engineered TiO₂, *Nat. Commun.* 13 (2022) 2806.
- [23] Z. Lu, M. He, L. Yang, Z. Ma, L. Yang, D. Wang, Y. Yan, W. Shi, Y. Liu, Z. Hua, Selective photodegradation of 2-mercaptobenzothiazole by a novel imprinted CoFe₂O₄/MWCNTs photocatalyst, *RSC Adv.* 5 (2015) 47820–47829.
- [24] Y. Xin, Y. Huang, K. Lin, Y. Yu, B. Zhang, Self-template synthesis of double-layered porous nanotubes with spatially separated photoredox surfaces for efficient photocatalytic hydrogen production, *Sci. Bull.* 63 (2018) 601–608.
- [25] Y. Wang, R. Godin, J.R. Durrant, J. Tang, Efficient Hole Trapping in Carbon Dot/Oxygen-Modified Carbon Nitride Heterojunction Photocatalysts for Enhanced Methanol Production from CO₂ under Neutral Conditions, *Angew. Chem., Int. Ed.* 60 (2021) 20811–20816.
- [26] L. Luo, L. Fu, H. Liu, Y. Xu, J. Xing, C.R. Chang, D.Y. Yang, J. Tang, Synergy of Pd atoms and oxygen vacancies on In₂O₃ for methane conversion under visible light, *Nat. Commun.* 13 (2022) 2930.
- [27] Z. Lu, B. Li, B. Wei, G. Zhou, Y. Xu, J. Zhang, H. Chen, S. Hua, C. Wu, X. Liu, NMP-induced surface self-corrosion-assisted rapid spin-coating method for synthesizing imprinted heterojunction photocatalyst anchored membrane towards high-efficiency selective degradation tetracycline, *Sep. Purif. Technol.* 314 (2023), 123609.
- [28] X. Xu, R. Wang, X. Sun, M. Lv, S. Ni, Layered Perovskite Compound NaLaTiO₄ Modified by Nitrogen Doping as a Visible Light Active Photocatalyst for Water Splitting, *ACS Catal.* 10 (2020) 9889–9898.
- [29] P. Chen, A. Khetan, F. Yang, V. Migunov, P. Weide, S.P. Stürmer, P. Guo, K. Kähler, W. Xia, J. Mayer, H. Pitsch, U. Simon, M. Muhler, Experimental and theoretical understanding of nitrogen-doping-induced strong metal-support interactions in Pd/TiO₂ catalysts for nitrobenzene hydrogenation, *ACS Catal.* 7 (2017) 1197–1206.
- [30] C. Foo, Y. Li, K. Lebedev, T. Chen, S. Day, C. Tang, S.C.E. Tsang, Characterisation of oxygen defects and nitrogen impurities in TiO₂ photocatalysts using variable-temperature X-ray powder diffraction, *Nat. Commun.* 12 (2021) 661.
- [31] T. Wu, P. Niu, Y. Yang, L.C. Yin, J. Tan, H. Zhu, J.T.S. Irvine, L. Wang, G. Liu, H. M. Cheng, Homogeneous doping of substitutional nitrogen/carbon in TiO₂ plates for visible light photocatalytic water oxidation, *Adv. Funct. Mater.* 29 (2019) 1901943.
- [32] K. Su, H. Liu, B. Zeng, Z. Zhang, N. Luo, Z. Huang, Z. Gao, F. Wang, Visible-light-driven selective oxidation of toluene into benzaldehyde over nitrogen-modified Nb₂O₅ nanomeshes, *ACS Catal.* 10 (2019) 1324–1333.
- [33] G. Zhou, Y. Cheng, Z. Yu, X. Liu, D. Chen, J. Wang, Y. Hang, Y. Xu, C. Li, Z. Lu, Regulation of coordination and doping environment via target molecular transformation for boosting selective photocatalytic ability, *Chem. Commun.* 58 (2022) 10036–10039.
- [34] Y. Shi, G. Zhan, H. Li, X. Wang, X. Liu, L. Shi, K. Wei, C. Ling, Z. Li, H. Wang, C. Mao, X. Liu, L. Zhang, Simultaneous Manipulation of Bulk Excitons and Surface Defects for Ultrasensitive and Highly Selective CO₂ Photoreduction, *Adv. Mater.* 33 (2021), e2100143.
- [35] H. Wang, D. Yong, S. Chen, S. Jiang, X. Zhang, W. Shao, Q. Zhang, W. Yan, B. Pan, Y. Xie, Oxygen-Vacancy-Mediated Exciton Dissociation in BiOBr for Boosting Charge-Carrier-Involved Molecular Oxygen Activation, *J. Am. Chem. Soc.* 140 (2018) 1760–1766.
- [36] Y. Shi, Z. Yang, L. Shi, H. Li, X. Liu, X. Zhang, J. Cheng, C. Liang, S. Cao, F. Guo, X. Liu, Z. Ai, L. Zhang, Surface Boronizing Can Weaken the Excitonic Effects of BiOBr Nanosheets for Efficient O₂ Activation and Selective NO Oxidation under Visible Light Irradiation, *Environ. Sci. Technol.* 56 (2022) 14478–14486.
- [37] Z. Lu, G. Zhou, B. Li, Y. Xu, P. Wang, H. Yan, M. Song, C. Ma, S. Han, X. Liu, Heterotopic reaction strategy for enhancing selective reduction and synergistic oxidation ability through trapping Cr (VI) into specific reaction site: A stable and self-cleaning ion imprinted CdS/HTNW photocatalytic membrane, *Appl. Catal., B* 301 (2022), 120787.
- [38] J. Chen, L. Lin, P. Lin, L. Xiao, L. Zhang, Y. Lu, W. Su, A direct Z-scheme Bi₂WO₆/La₂Ti₂O₇ Photocatalyst for Selective Reduction of CO₂ to CO, *Chin. J. Struct. Chem.* (2022), 100010.
- [39] L. Chang, Y. Pu, P. Jing, J. Ji, X. Wei, B. Cao, Y. Yu, S. Xu, H. Xie, Z-Scheme CuWO₄/BiOCl photocatalysts with oxygen vacancy as electron mediator for boosted photocatalytic degradation of norfloxacin, *Surf. Interfaces* 31 (2022), 102010.
- [40] W. Xing, L. Ni, X. Liu, Y. Luo, Z. Lu, Y. Yan, P. Huo, Synthesis of thermal-responsive photocatalysts by surface molecular imprinting for selective degradation of tetracycline, *RSC Adv.* 3 (2013) 26334–26342.
- [41] B. Zhao, X. Huang, Y. Ding, Y. Bi, Bias-Free Solar-Driven Syngas Production: A Fe₂O₃ Photoanode Featuring Single-Atom Cobalt Integrated with a Silver-Palladium Cathode, *Angew. Chem., Int. Ed.* 135 (2023), e202213067.
- [42] T.D. Kühne, M. Iannuzzi, M. Del Ben, V.V. Rybkin, P. Seewald, F. Stein, T. Laino, R. Z. Khaliullin, O. Schütt, F. Schiffmann, CP2K: An electronic structure and molecular dynamics software package-Quickstep: Efficient and accurate electronic structure calculations, *J. Chem. Phys.* 152 (2020), 194103.
- [43] Y. Shi, J. Li, D. Huang, X. Wang, Y. Huang, C. Chen, R. Li, Specific adsorption and Efficient Degradation of Cylindrospermopsin on Oxygen-Vacancy Sites of BiOBr, *ACS Catal.* 13 (2022) 445–458.
- [44] J. Wu, X. Li, W. Shi, P. Ling, Y. Sun, X. Jiao, S. Gao, L. Liang, J. Xu, W. Yan, C. Wang, Y. Xie, Efficient Visible-Light-Driven CO₂ Reduction Mediated by Defect-Engineered BiOBr Atomic Layers, *Angew. Chem., Int. Ed.* 57 (2018) 8719–8723.
- [45] Y.V. Divyasri, N. Lakshmana Reddy, K. Lee, M. Sakar, V. Navakoteswara Rao, V. Venkatramu, M.V. Shankar, N.C. Gangi Reddy, Optimization of N doping in TiO₂ nanotubes for the enhanced solar light mediated photocatalytic H₂ production and dye degradation, *Environ. Pollut.* 269 (2021), 116170.
- [46] D. Tan, J. Zhang, J. Shi, S. Li, B. Zhang, X. Tan, F. Zhang, L. Liu, D. Shao, B. Han, Photocatalytic CO₂ transformation to CH₄ by Ag/Pd bimetal supported on N-doped TiO₂ nanosheet, *ACS Appl. Mater. Interfaces* 10 (2018) 24516–24522.
- [47] Z. Lu, G. Zhou, M. Song, X. Liu, H. Tang, H. Dong, P. Huo, F. Yan, P. Du, G. Xing, Development of magnetic imprinted PEDOT/CdS heterojunction photocatalytic nanoreactors: 3-Dimensional specific recognition for selectively photocatalyzing danofloxacin mesylate, *Appl. Catal., B* 268 (2020), 118433.
- [48] X. Yu, X. Gao, Z. Lu, X. Liu, P. Huo, X. Liu, D. Wu, Y. Yan, Preparation and photodegradation properties of transition metal ion-poly-o-phenylenediamine/TiO₂/fly-ash cenospheres by ion imprinting technology, *RSC Adv.* 3 (2013) 14807–14813.
- [49] G. Jiang, X. Li, Z. Wei, T. Jiang, X. Du, W. Chen, Effects of N and/or S doping on structure and photocatalytic properties of BiOBr crystals, *Acta Metall. Sin. (Engl. Lett.)* 28 (2015) 460–466.
- [50] Y. Zhou, Y. Zhang, M. Lin, J. Long, Z. Zhang, H. Lin, J.C. Wu, X. Wang, Monolayered Bi₂WO₆ nanosheets mimicking heterojunction interface with open surfaces for photocatalysis, *Nat. Commun.* 6 (2015) 8340.
- [51] J. Xie, H. Xie, B.L. Su, Y.B. Cheng, X. Du, H. Zeng, M. Wang, W. Wang, H. Wang, Z. Fu, Mussel-Directed Synthesis of Nitrogen-Doped Anatase TiO₂, *Angew. Chem., Int. Ed.* 55 (2016) 3031–3035.
- [52] S. Sun, P. Gao, Y. Yang, P. Yang, Y. Chen, Y. Wang, N-doped TiO₂ nanobelts with coexposed (001) and (101) facets and their highly efficient visible-light-driven photocatalytic hydrogen production, *ACS Appl. Mater. Interfaces* 8 (2016) 18126–18131.
- [53] Y. Song, N. Li, D. Chen, Q. Xu, H. Li, J. He, J. Lu, N-Doped and CdSe-Sensitized 3D-Ordered TiO₂ Inverse Opal Films for Synergistically Enhanced Photocatalytic Performance, *ACS Sustain. Chem. Eng.* 6 (2018) 4000–4007.
- [54] Y. Huang, Z. Guo, H. Liu, S. Zhang, P. Wang, J. Lu, Y. Tong, Heterojunction architecture of N-doped WO₃ nanobundles with Ce₂S₃ nanodots hybridized on a carbon textile enables a highly efficient flexible photocatalyst, *Adv. Funct. Mater.* 29 (2019) 1903490.
- [55] Y. Zhao, Y. Zhu, J. Zhu, H. Wang, Z. Ma, L. Gao, Y. Liu, K. Yang, Y. Shu, J. He, Atomic-resolution investigation of structural transformation caused by oxygen vacancy in La_{0.9}Sr_{0.1}TiO₃₊ titanate layer perovskite ceramics, *J. Mater. Sci. Technol.* 104 (2022) 172–182.
- [56] Z. Huang, T. Xiong, X. Lin, M. Tian, W. Zeng, J. He, M. Shi, J. Li, G. Zhang, L. Mai, S. Mu, Carbon dioxide directly induced oxygen vacancy in the surface of lithium-rich layered oxides for high-energy lithium storage, *J. Power Sources* 432 (2019) 8–15.
- [57] Z. Lu, G. Zhou, M. Song, D. Wang, P. Huo, W. Fan, H. Dong, H. Tang, F. Yan, G. Xing, Magnetic functional heterojunction reactors with 3D specific recognition for selective photocatalysis and synergistic photodegradation in binary antibiotic solutions, *J. Mater. Chem. A* 7 (2019) 13986–14000.
- [58] F. Chang, H. Chen, X. Zhang, B. Lei, X. Hu, N-p heterojunction Bi₄O₅I₂/Fe₃O₄ composites with efficiently magnetic recyclability and enhanced visible-light-driven photocatalytic performance, *Sep. Purif. Technol.* 238 (2020), 116442.
- [59] S. Gao, C. Guo, S. Hou, L. Wan, Q. Wang, J. Lv, Y. Zhang, J. Gao, W. Meng, J. Xu, Photocatalytic removal of tetrabromobisphenol A by magnetically separable flower-like BiOBr/BiOI/Fe₃O₄ hybrid nanocomposites under visible-light irradiation, *J. Hazard. Mater.* 331 (2017) 1–12.
- [60] Z. Lu, X. Zhao, Z. Zhu, M. Song, N. Gao, Y. Wang, Z. Ma, W. Shi, Y. Yan, H. Dong, A novel hollow capsule-like recyclable functional ZnO/C/Fe₃O₄ endowed with three-dimensional oriented recognition ability for selectively photodegrading danofloxacin mesylate, *Catal. Sci. Technol.* 6 (2016) 6513–6524.

- [61] R. Kang, S. Park, Y.K. Jung, D.C. Lim, M.J. Cha, J.H. Seo, S. Cho, High-efficiency polymer homo-tandem solar cells with carbon quantum-dot-doped tunnel junction intermediate layer, *Adv. Energy Mater.* 8 (2018) 1702165.
- [62] J. Chen, H. Che, K. Huang, C. Liu, W. Shi, Fabrication of a ternary plasmonic photocatalyst CQDs/Ag/Ag₂O to harness charge flow for photocatalytic elimination of pollutants, *Appl. Catal., B* 192 (2016) 134–144.
- [63] Z. Wang, F. Yuan, X. Li, Y. Li, H. Zhong, L. Fan, S. Yang, 53% Efficient red emissive carbon quantum dots for high color rendering and stable warm white-light-emitting diodes, *Adv. Mater.* 29 (2017) 1702910.
- [64] S. Chen, Y. Hu, S. Meng, X. Fu, Study on the separation mechanisms of photogenerated electrons and holes for composite photocatalysts g-C₃N₄-WO₃, *Appl. Catal., B* 150–151 (2014) 564–573.
- [65] S. Meng, J. Zhang, S. Chen, S. Zhang, W. Huang, Perspective on construction of heterojunction photocatalysts and the complete utilization of photogenerated charge carriers, *Appl. Surf. Sci.* 476 (2019) 982–992.
- [66] Y. Lu, Y. Yang, X. Fan, Y. Li, D. Zhou, B. Cai, L. Wang, K. Fan, K. Zhang, Boosting Charge Transport in BiVO₄ Photoanode for Solar Water Oxidation, *Adv. Mater.* 34 (2022), e2108178.
- [67] L. Liu, H. Meng, Y. Chai, X. Chen, J. Xu, X. Liu, W. Liu, D.M. Guldi, Y. Zhu, Enhancing Built-in Electric Fields for Efficient Photocatalytic Hydrogen Evolution by Encapsulating C(60) Fullerene into Zirconium-Based Metal-Organic Frameworks, *Angew. Chem., Int. Ed.* (2023), e202217897.
- [68] Z. Guo, Y. Wan, M. Yang, J. Snider, K. Zhu, L. Huang, Long-range hot-carrier transport in hybrid perovskites visualized by ultrafast microscopy, *Science* 356 (2017) 59–62.
- [69] R. Lai, Y. Liu, X. Luo, L. Chen, Y. Han, M. Lv, G. Liang, J. Chen, C. Zhang, D. Di, G. D. Scholes, F.N. Castellano, K. Wu, Shallow distance-dependent triplet energy migration mediated by endothermic charge-transfer, *Nat. Commun.* 12 (2021) 1532.
- [70] Z.B. Fang, T.T. Liu, J. Liu, S. Jin, X.P. Wu, X.Q. Gong, K. Wang, Q. Yin, T.F. Liu, R. Cao, H.C. Zhou, Boosting Interfacial Charge-Transfer Kinetics for Efficient Overall CO₂ Photoreduction via Rational Design of Coordination Spheres on Metal-Organic Frameworks, *J. Am. Chem. Soc.* 142 (2020) 12515–12523.
- [71] L. Sun, X. He, S. Zeng, Y. Yuan, R. Li, W. Zhan, J. Chen, X. Wang, X. Han, Double Insurance of Continuous Band Structure and N-C Layer Induced Prolonging of Carrier Lifetime to Enhance the Long-Wavelength Visible-Light Catalytic Activity of N-Doped In₂O₃, *Inorg. Chem.* 60 (2021) 1160–1171.
- [72] F. Wang, X. He, L. Sun, J. Chen, X. Wang, J. Xu, X. Han, Engineering an N-doped TiO₂@N-doped C butterfly-like nanostructure with long-lived photo-generated carriers for efficient photocatalytic selective amine oxidation, *J. Mater. Chem. A* 6 (2018) 2091–2099.
- [73] G. Zhou, H. Yan, Y. Ren, M. Song, Y. Hang, X. Liu, C. Li, S. Han, Z. Chen, Z. Lu, Construction of internal electric field in imprinted poly (ionic liquid)-TiO₂ composite nanoreactor for improving hole directional enrichment and selective photodegradation, *Compos. Sci. Technol.* 228 (2022), 109657.
- [74] S. Huang, Y. Wang, J. Wan, Z. Yan, Y. Ma, G. Zhang, S. Wang, Ti₃C₂T_x as electron-hole transfer mediators to enhance AgBr/BiOBr Z heterojunction photocatalytic for the degradation of Tetrabromobisphenol A: Mechanism Insight, *Appl. Catal., B* 319 (2022), 121913.
- [75] S. Zhang, Z. Zhang, Y. Si, B. Li, F. Deng, L. Yang, X. Liu, W. Dai, S. Luo, Gradient Hydrogen Migration Modulated with Self-Adapting S Vacancy in Copper-Doped ZnIn₂S₄ Nanosheet for Photocatalytic Hydrogen Evolution, *ACS Nano* 15 (2021) 15238–15248.
- [76] E. Wang, A. Mahmood, S.-G. Chen, W. Sun, T. Muhmood, X. Yang, Z. Chen, Solar-Driven Photocatalytic Reforming of Lignocellulose into H₂ and Value-Added Biochemicals, *ACS Catal.* 12 (2022) 11206–11215.
- [77] I. Nabi, A.U. Bacha, K. Li, H. Cheng, T. Wang, Y. Liu, S. Ajmal, Y. Yang, Y. Feng, L. Zhang, Complete photocatalytic mineralization of microplastic on TiO₂ nanoparticle film, *iScience* 23 (2020), 101326.
- [78] R. Nadarajan, W.A.W.A. Bakar, S. Toemen, M.A. Habib, N.A. Eleburuike, Structure-activity relationship of TiO₂ based trimetallic oxide towards 1,2-dichlorobenzene photodegradation: Influence of preparation method and its mechanism, *Chem. Eng. J.* 351 (2018) 708–720.
- [79] X. Yan, W. Sun, L. Fan, P.N. Duchesne, W. Wang, C. Kubel, D. Wang, S.G.H. Kumar, Y.F. Li, A. Tavasoli, T.E. Wood, D.L.H. Hung, L. Wan, L. Wang, R. Song, J. Guo, I. Gourevich, A.A. Jelle, J. Lu, R. Li, B.D. Hatton, G.A. Ozin, Nickel@Siloxene catalytic nanosheets for high-performance CO₂ methanation, *Nat. Commun.* 10 (2019) 2608.